

An Oxygen-Vacancy-Rich Semiconductor-Supported Bifunctional Catalyst for Efficient and Stable Zinc–Air Batteries

Guihua Liu, Jingde Li, Jing Fu, Gaopeng Jiang, Gregory Lui, Dan Luo, Ya-Ping Deng, Jing Zhang, Zachary P. Cano, Aiping Yu, Dong Su, Zhengyu Bai,* Lin Yang, and Zhongwei Chen*

The highly oxidative operating conditions of rechargeable zinc–air batteries causes significant carbon-support corrosion of bifunctional oxygen electrocatalysts. Here, a new strategy for the catalyst support design focusing on oxygen vacancy (OV)-rich, low-bandgap semiconductor is proposed. The OVs promote the electrical conductivity of the oxide support, and at the same time offer a strong metal–support interaction (SMSI), which enables the catalysts to have small metal size, high catalytic activity, and high stability. The strategy is demonstrated by successfully synthesizing ultrafine Co-metal-decorated 3D ordered macroporous titanium oxynitride (3DOM-Co@TiO_xN_y). The 3DOM-Co@TiO_xN_y catalyst exhibits comparable activities for oxygen reduction and evolution reactions, but much higher cycling stability than noble metals in alkaline conditions. The zinc–air battery using this catalyst delivers an excellent stability with less than 1% energy efficiency loss over 900 charge–discharge cycles at 20 mA cm⁻². The high stability is attributed to the strong SMSI between Co and 3DOM-TiO_xN_y which is verified by density functional theory calculations. This work sheds light on using OV-rich semiconductors as a promising support to design efficient and durable nonprecious electrocatalysts.

The practical application of rechargeable zinc–air batteries requires a low-cost, efficient, and stable air electrode catalyst toward both the oxygen reduction reaction (ORR) and oxygen evolution reaction (OER). The most promising nonprecious bifunctional catalysts are carbon-supported transition metal hybrid materials.^[1] However, carbon-supported catalysts suffer from carbon electrochemical oxidation, which causes the loss or aggregation of supported catalysts and degrades the electrocatalysis durability and performance.^[2] To alleviate this problem, some strategies have been reported including coating the carbon support with corrosion-resistant TiO₂,^[3] using conductive TiN as an alternative support,^[4] or developing perovskite oxides as active catalysts.^[5] However, both TiO₂ and perovskite oxides have an intrinsic low-conductivity drawback, and nor TiN is an optimum support material to obtain highly dispersed and active catalysts due to the nondefective surface structure. Thus, the objective of this study is to

develop a conductive and oxidation-resistant support to relieve catalyst degradation, and at the same time achieve a high bifunctional catalytic activity with enhanced durability performance.

Here, we propose that OV-rich, low-bandgap oxide semiconductor can be a promising support to design active and durable ultrafine metal catalysts in electrocatalysis (**Figure 1a**). This argument is built on our multidisciplinary understanding of OVs in semiconductor physics and heterogeneous solid–gas catalysis: i) the OVs lower the bandgap in oxide semiconductors: the higher the OV concentration, the higher the conductivity of the oxides^[6]; ii) in solid–gas catalysis, the OVs on oxide supports would provide a strong metal–support interaction (SMSI) with the supported metal catalysts and results in high metal dispersion, small metal size, high relative catalytic activity, and high stability.^[7] That is, the OVs are not only beneficial for the conductivity of the oxides, but also offer an SMSI that favors the formation and stabilization of highly active ultrafine metal nanoparticles. Note that, in electrocatalysis, the role of OVs in metal oxides as active components is well reported for contributing to its enhanced catalytic activities.^[8] However, the

G. Liu, Dr. J. Li, Dr. J. Fu, Dr. G. Jiang, G. Lui, D. Luo, Y.-P. Deng, J. Zhang, Z. P. Cano, Prof. A. Yu, Prof. Z. Chen
Department of Chemical Engineering
Waterloo Institute for Nanotechnology
Waterloo Institute for Sustainable Energy
University of Waterloo
Waterloo, Ontario N2L 3G1, Canada
E-mail: zhwenchen@uwaterloo.ca

Dr. D. Su
Center for Functional Nanomaterials
Brookhaven National Laboratory
Upton, NY 11953, USA

Prof. Z. Bai, Prof. L. Yang
School of Chemistry and Chemical Engineering
Key Laboratory of Green Chemical Media and Reactions
Ministry of Education
Henan Normal University
Xinxiang 453007, China
E-mail: baizhengyu@htu.cn

 The ORCID identification number(s) for the author(s) of this article can be found under <https://doi.org/10.1002/adma.201806761>.

DOI: 10.1002/adma.201806761

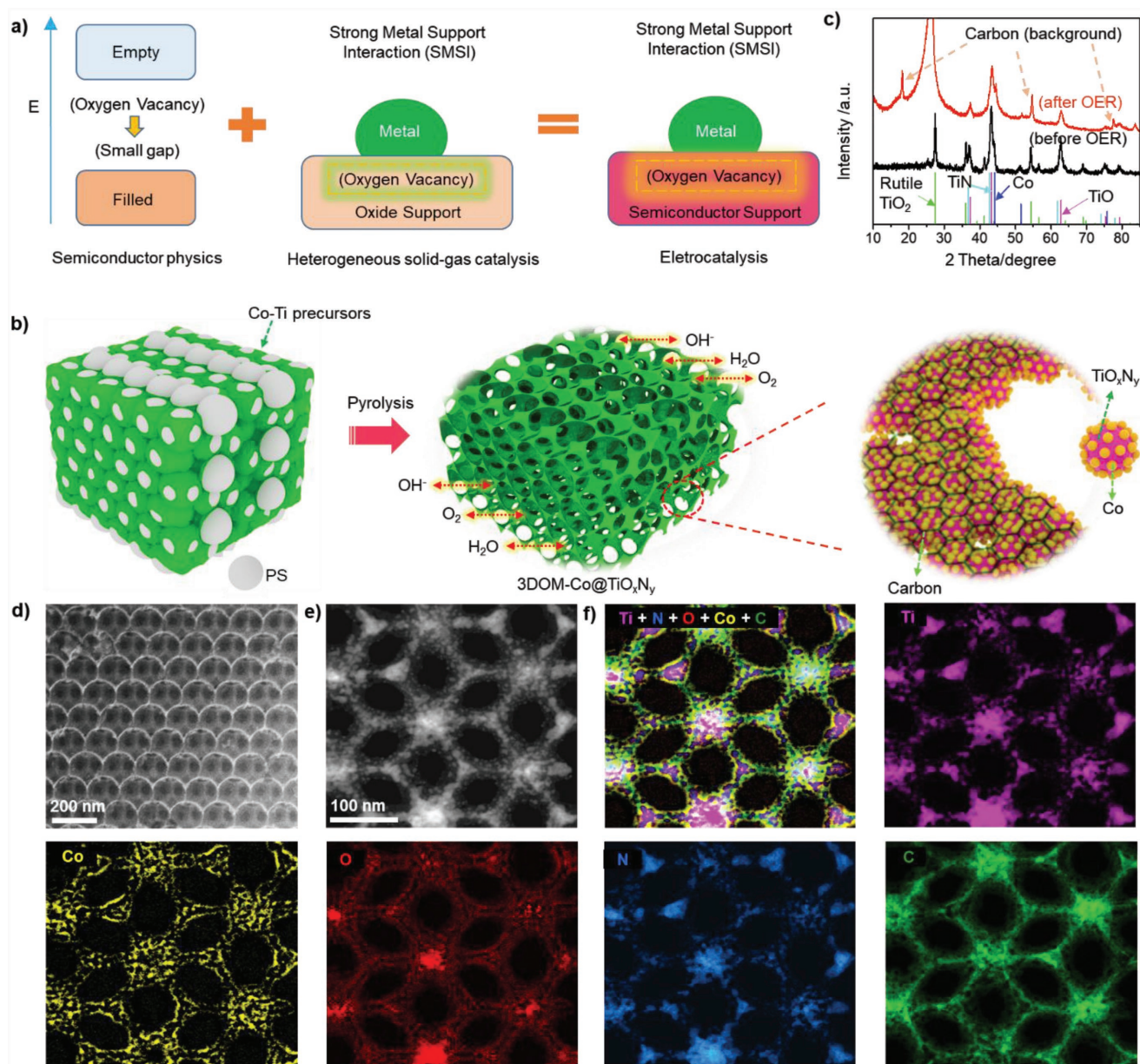


Figure 1. a) The designing strategy for semiconductor-supported metal as electrocatalysts; b) schematic of preparation procedure for 3DOM-Co@TiO_xN_y catalyst, and the Co interface-confinement effect induced by SMSI and carbon layer; c) XRD patterns of 3DOM-Co@TiO_xN_y before and after OER reaction; d) SEM; e) STEM image; and f) STEM-electron energy-loss spectroscopy (STEM-EELS) elemental mapping (Ti, Co, O, N, and C) of 3DOM-Co@TiO_xN_y.

significance of OVs in supporting materials is much less discussed, in particular for processes involving the oxidative OER reaction. To the best of our knowledge, this is the first time that the concept of OV-induced SMSI is introduced to design active and stable semiconductor-based electrocatalysts with ultrafine dispersion of the active phase for ORR and OER.

In this work, we developed an efficient and durable bifunctional catalyst which comprises OV-rich 3DOM TiO_xN_y supported ultrafine Co (Figure 1b), referred to as 3DOM-Co@TiO_xN_y. It was prepared by thermal treating polystyrene (PS) template soaked with cobalt acetate [Co(CH₃COO)₂·4H₂O] and titanium butoxide [Ti(OBu)₄] precursor solution with an atomic

ratio of Co:Ti = 1:20 (Figures S1 and S2, Supporting Information). At different heating stages, Ar and NH₃ atmosphere were used. This ensures an oxygen-deficient and reductive environment that is beneficial for OVs formation in the TiO_xN_y support. Detailed synthesis procedures can be found in the Supporting Information. It should be mentioned that the calcination of PS beads not only forms the 3DOM morphology, but also generates a N-doped carbonaceous layer enwrapping the Co@TiO_xN_y framework. Such N-doped carbon layer is mainly introduced to improve the ORR activity of the composite^[9] rather than as conductive supporting material. The carbon layer also provides further confinement for ultrafine Co metal catalyst on TiO_xN_y

(Figure 1b), which is discussed later. The crystal components of $\text{Co@TiO}_x\text{N}_y$ were identified as metallic Co, TiO, TiN, and rutile TiO_2 through X-ray diffraction (XRD) analysis (Figure 1c, before OER). For the sake of comparison, 3DOM composites without the addition of Co precursor or ammonolysis treatment were also developed. The resulting products were identified and referred to as 3DOM-TiON and 3DOM-Co@ TiO_x (Ar), respectively (Figure S3, Supporting Information).

Figure 1d shows the 3DOM morphology of the composite: it has macroporous pores of ≈ 150 nm and interconnected walls, providing a strong structural support for the composite. Interestingly, the 3DOM-Co@ TiO_xN_y was found featured with a IV type N_2 absorption-desorption isotherm,^[10] as shown in Figure S4 (Supporting Information). This indicates that, in addition to the macropores, it also contains mesopores, leading to a high Brunauer-Emmett-Teller (BET) surface area of $266 \text{ m}^2 \text{ g}^{-1}$. Together with its 3DOM porous structure, the high surface area ensures high availability of active sites and low-mass transfer resistance within the catalyst, which are beneficial for the electrochemical performance of the catalyst. Scanning transmission electron microscopy (STEM) image of Figure 1e shows that the 3DOM interconnected walls are built by aggregated nanoparticles. High-magnification electron energy-loss spectroscopy (EELS) mapping (Figure 1f) confirms these nanoparticles are TiO_xN_y with their outer surfaces homogeneously covered with Co (atomic composition of 0.79%; Table S1, Supporting Information), thus appearing to exhibit the “core-shell” structure (Figure 2a). The high-resolution TEM (HRTEM) image and the corresponding FFT pattern further confirm the existence of ultrafine metallic Co phase on TiO_xN_y (Figure S5, Supporting Information). Additionally, one can see that C element is uniformly distributed on the outermost surface layer of the $\text{Co@TiO}_x\text{N}_y$ particles, suggesting there is a carbon layer covering the 3DOM walls. This carbon layer not only improves the conductivity of the composite but may also act like a confining layer to restrict ultrafine Co onto TiO_xN_y , and therefore can further contribute to the stability of the 3DOM-Co@ TiO_xN_y . To distinguish the contribution of carbon layer and TiO_xN_y components to the composite conductivity, the electrical conductivity of 3DOM-Co@ TiO_xN_y and 3DOM-Co@ TiO_x (Ar) was measured. Both of the composites have a carbon layer. However, the conductivity of 3DOM-Co@ TiO_xN_y (5.11 S cm^{-1}) is 1 order of magnitude higher than that of 3DOM-Co@ TiO_x (Ar) (0.76 S cm^{-1}), as shown in Figure 2b. This shows that the conductivity of the 3DOM-Co@ TiO_xN_y composite is mainly contributed by TiO_xN_y rather than the carbon layer. All of these observations strongly support the successful synthesis of ultrafine Co on conductive TiO_xN_y .

The local chemical environment on the surface of 3DOM-Co@ TiO_xN_y (before OER) was examined by X-ray photoelectron spectroscopy (XPS). Its Ti 2p spectrum was deconvoluted into three overlapping doublets (Figure 2c). The minor Ti $2p_{3/2}$ peak located at 455.2 eV can be assigned to TiN or TiO. The other two peaks centered at 456.8 and 458.3 eV are referred to TiON and reduced TiO_{2-x} or Ti_2O_3 , respectively.^[11] The Ti $2p_{3/2}$ signal at 459.1 eV associated with TiO_2 is very weak, which confirms the low oxidation state of Ti in TiO_xN_y . The Co 2p spectrum of 3DOM-Co@ TiO_xN_y has a characteristic $2p_{3/2}$ peak of CoO rather than metallic Co, suggesting that the ultrafine Co was mildly oxidized in the air

(Figure 2d). The N 1s spectrum shows the existence of N-Ti-O (396.2 eV), N-Ti (397.2 eV), and N-C components in TiO_xN_y ^[12] (Figure 2e). The OVs in 3DOM-Co@ TiO_xN_y was probed by the O 1s XPS spectrum (Figure 2f). The peak at 530.1 eV is associated with lattice O^{2-} from O-Ti or O-Co bond,^[13] the peak at 531.6 eV represents the nonlattice (defective) O^{2-} or OH species.^[14] Although the formation of OH species on the catalyst surface is possible, e.g., its exposure to the ambient atmosphere, the defective O^{2-} is consistent with the wide distribution of Ti^{2+} , Ti^{3+} , and Ti^{4+} states in the Ti 2p spectrum (Figure 2c), indicative of an enrichment of OVs on the TiO_xN_y surface. The locations of OV can be distributed across both of the TiO and the TiO_2 lattice of TiO_xN_y . This is because i) TiO itself is commonly featured with high OV content (11–20%)^[15]; ii) TiO_2 with OV has been reported to be obtained in a low-oxygen atmosphere,^[6] therefore the existence of OV in TiO and TiO_2 lattice obtained under the strong reducing atmosphere of NH_3 is inevitable. Further evidence comes from a close inspection of the shape of the O-K (O 1s \rightarrow 2p) and Ti-L (Ti 2p \rightarrow 3d) core edges of EELS spectrum of 3DOM-Co@ TiO_xN_y (Figure 2g), which provides chemical and electronic information on buried atoms that are in a bulk-like environment.^[16] The O-K edge fine structure has been reported sensitive to O-O ordering and damps out as the OV concentration increases.^[17] As shown in Figure 2g, the O-K edge fine structure “washes out” in 3DOM-Co@ TiO_xN_y compared with that of 3DOM-Co@ TiO_x (Ar), indicating the high OV concentration in TiO_xN_y . This is also consistent with the distinct peak shift in the Ti-L edge toward low photon energy, as OVs are electron donors. The Co-L edge signal is not apparent, supportive for the low loading of Co (0.79%) on TiO_xN_y .

The beneficial effect of OVs in SMSI within Co- TiO_xN_y was supported by density functional theory (DFT) calculations (Figure 3a; Figure S6, Supporting Information). Here, TiO_2 and TiO surfaces were used as representative crystals for 3DOM-Co@ TiO_xN_y because they are the two main crystalline oxides in TiO_xN_y observed in our pre- and post-OER XRD analysis (Figure 1c). The Ti-N component is neglected to simplify the DFT model. This is a reasonable assumption because we only focus on the OV sites. The (110) and (100) surfaces are used to model the TiO_x oxides because they are the reported stable surfaces on rutile TiO_2 ,^[18] and featured planes for TiO as well. The adhesion energy of tetrahedral Co_4 cluster on the OV sites of nonstoichiometric cubic TiO and rutile TiO_2 (110) surfaces is 12.13 and 12.98 eV, respectively, indicative of the SMSI. In addition, we found that, for (110) surface, the 3D Co_4 cluster was stable only on the nonstoichiometric (reduced) surfaces, whereas distortion of the Co_4 cluster occurs on the stoichiometric surface (Figure 3a). For instance, on the stoichiometric TiO_2 (110) surface, although it has a much higher adhesion energy (19.65 eV) than that on reduced rutile TiO_2 (110), the severe distortion of Co_4 cluster results in many Co-O bonds, suggesting that the stoichiometric TiO_2 (110) surface is not favorable for the nucleation of metallic Co. On the (100) of TiO_2 and TiO, the tetrahedral structure of Co_4 cluster is preserved, and the nonstoichiometric (reduced) TiO_2 and TiO exhibit stronger SMSI than that on stoichiometric model (Figure S6, Supporting Information). Moreover, we found that on both of the reduced (110) and (100) surfaces, the Co tends to incorporate into the TiO_2 and TiO lattice, revealing that the

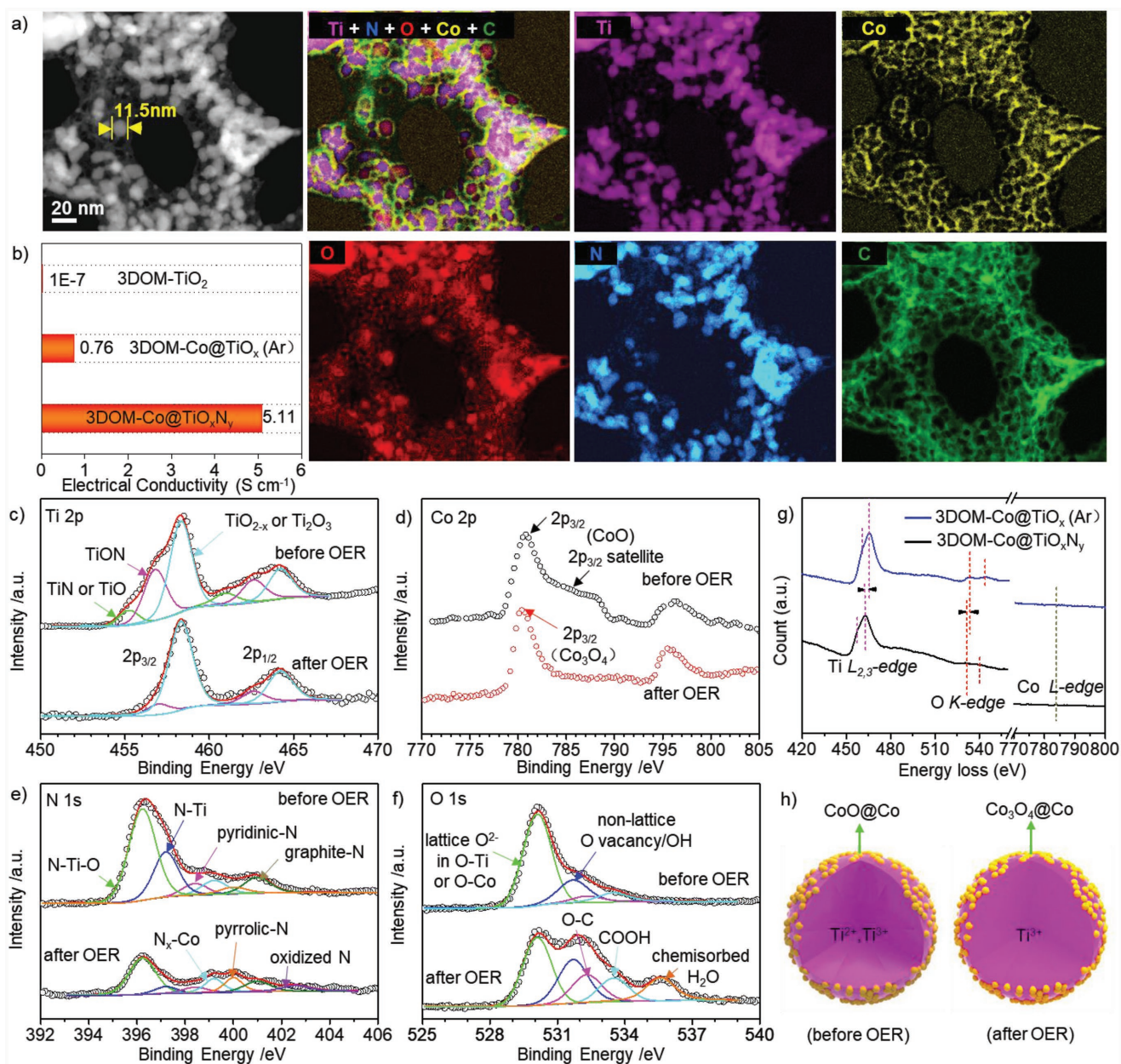


Figure 2. a) STEM image and high-magnification STEM-EELS mapping of Ti, Co, O, N, and C elements; b) electrical conductivity; c) Ti 2p; d) Co 2p; e) N 1s; and f) O 1s XPS spectrum of 3DOM-Co@TiO_xN_y before and after 16 h of OER half-cell test at a constant potential of 1.60 V versus RHE; g) comparison of EELS spectra of Ti-L, O-K, and Co-L core edges acquired from the as-prepared 3DOM composites; h) schematic showing the changes of Ti 2p and Co 2p states before and after 16 h of OER reaction.

OV acts as sites for the Co nuclei. Thus, we can further infer that, in addition to providing an SMSI, OV sites on the reduced surfaces also act as nucleation sites for Co growth during calcination. That is, the OV sites are essential in the nucleation and stabilization of the ultrafine metals. This is also supported by the fact that surface defects acting as preferred nucleation sites for the growth of metal particles have been widely recognized.^[19]

The electrocatalytic activities of the 3DOM composites were evaluated by linear sweep voltammetry (LSV) with 0.1 M KOH solution. Figure 3b shows that 3DOM-Co@TiO_xN_y delivers an ORR onset potential of 0.90 V (vs RHE). Although its

onset potential still cannot catch up with that of Pt/C catalyst (0.98 V), 3DOM-Co@TiO_xN_y exhibits a comparable ORR half-wave potential (0.84 V) to that of Pt/C (0.85 V). Meanwhile, it also shows much higher ORR activity than the Co-free 3DOM-TiON and N-free 3DOM-Co@TiO_x(Ar). The linearity of the K-L plot and the number of electrons ($n = 4.0$) transferred during ORR also indicate fast kinetics throughout the potential range inspected (Figure S7a,b, Supporting Information). In the case of OER, 3DOM-Co@TiO_xN_y exhibits the highest activity among the 3DOM composites (Figure 3c). For example, when a current density of 10 mA cm⁻² is generated, it has a similar OER

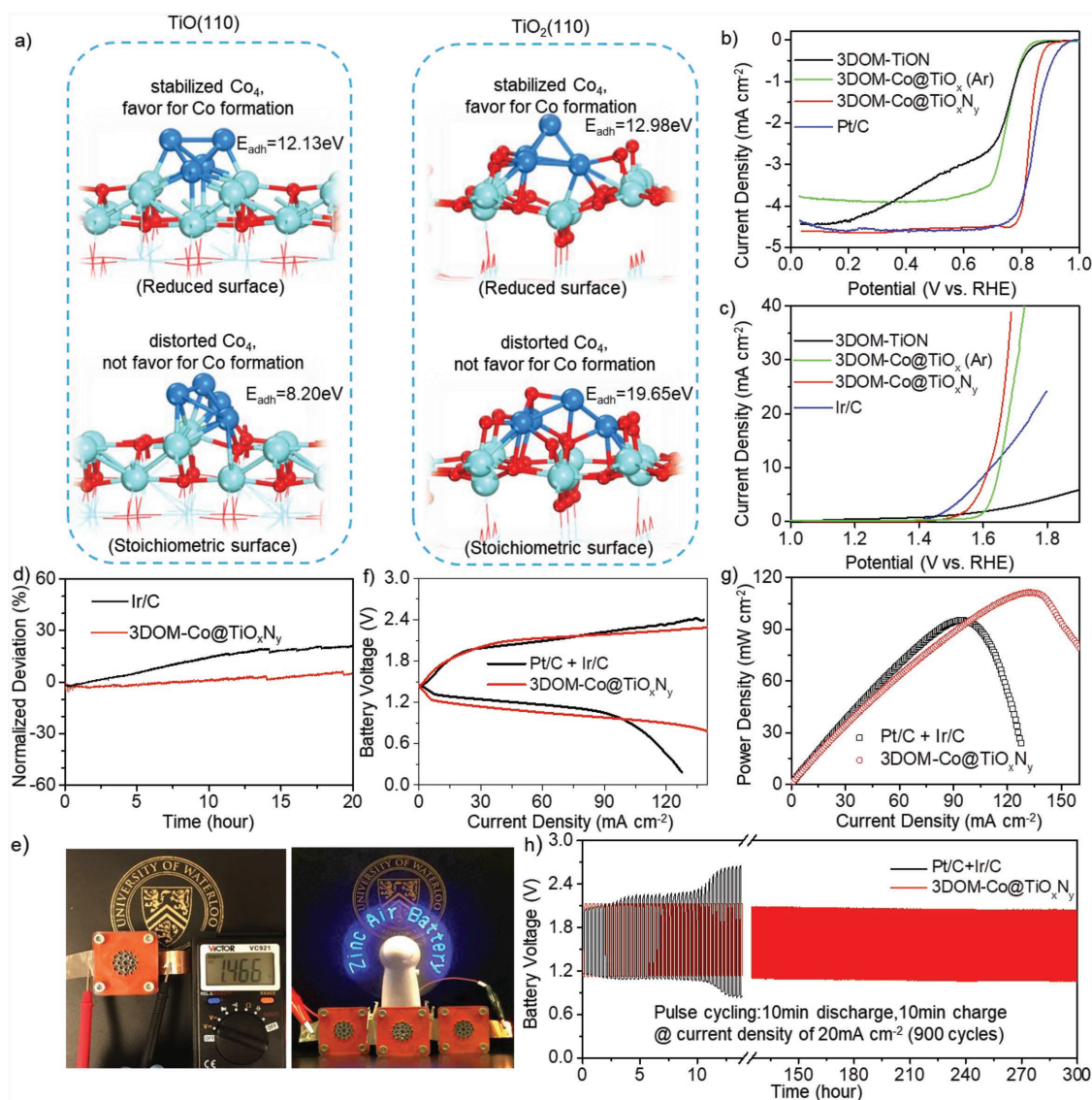


Figure 3. a) The most stable geometries and the corresponding adhesion energy of Co₄ cluster on reduced and stoichiometric TiO and TiO₂ (110) surface: blue (Co), cyan (Ti), red (O); b) ORR and c) OER LSV curves of various 3DOM composites obtained at a scan rate of 10 mV s⁻¹ in 0.1 M KOH electrolyte at 900 and 1600 rpm, respectively; d) long-term OER electrolysis stability under constant current density at 10 mA cm⁻²; e) demonstration of the zinc–air battery configuration; f) charge and discharge polarization curves; g) power density plots; and h) cycling performance of zinc–air batteries assembled using 3DOM-Co@TiO_xN_y and Pt/C+Ir/C as air electrodes in ambient air.

overpotential (≈ 385 mV) as that of commercial Ir/C, whereas the overpotential for N-free 3DOM-Co@TiO_x (417 mV) is slightly higher. The Co-free 3DOM-TiON composite has only minor OER activity, suggesting Co is the active component for OER. The high ORR and OER activity of 3DOM-Co@TiO_xN_y was further confirmed by its Tafel plot (Figure S7c,d, Supporting Information). The OER activities of these as-developed catalysts normalized by the electrochemically active surface area (ECSA) also show a similar trend (Figures S8 and S9, Supporting Information), revealing that the activity enhancement of 3DOM-Co@TiO_xN_y is mainly due to an increase in intrinsic surface specific activity of 3DOM-Co@TiO_xN_y. Note that, for comprehensive comparison, three other 3DOM composites, including oxidized 3DOM-Co₃O₄@TiO₂ (air-annealed

3DOM-Co@TiO_xN_y), Co@TiO_xN_y (in NH₃ 10 min), and Co@TiO_xN_y (in NH₃ 1 h), were also synthesized and characterized (Figures S3 and S10, Supporting Information). Figure S11 (Supporting Information) shows that all the three Co@TiO_xN_y composites treated by NH₃ exhibit higher catalytic activities for both ORR and OER than the oxidized Co₃O₄@TiO₂, indicating the positive effect of N present in the Co@TiO_xN_y catalysts. Moreover, despite all three catalysts having similar ORR activities, the Co@TiO_xN_y (which underwent 40 min NH₃ treatment) provides the most favorable degree of oxygen vacancies that allow for the highest OER activity.

The stability of the catalyst was examined by performing a CP test at 10 mA cm⁻². It shows that 3DOM-Co@TiO_xN_y electrode exhibits a much more stable voltage–time curve

than Ir/C under OER: its output voltage increased by 5% after 20 h operation, much lower than that of Ir/C (20%), as shown in Figure 3d. When fabricated into an air electrode in a rechargeable zinc–air battery, an open circuit voltage of ≈ 1.47 V is achieved (Figure 3e). At 1.0 V, the battery delivers a discharge current density of 95 mA cm^{-2} (Figure 3f). Notably, at low voltages under 0.8 V, 3DOM-Co@Ti_xON_y was able to deliver a much higher current density than that of Pt/C+Ir/C catalyst mixture, confirming the enhanced mass transfer realized by its 3DOM structure. Additionally, Figure 3g shows that it reaches a peak power density of 110 mW cm^{-2} at a current density of 135 mA cm^{-2} (0.80 V), higher than that of Pt/C+Ir/C catalyst mixture. The specific capacity of a primary zinc–air battery with 3DOM-Co@Ti_xON_y catalyst was found to be 697 mAh g^{-1} (Figure S12, Supporting Information), and the corresponding energy density is 865 Wh kg^{-1} , which are comparable to previously reported work.^[20] The battery stabilities using Pt/C+Ir/C and 3DOM-Co@Ti_xON_y electrodes were further examined at a current density of 20 mA cm^{-2} with each cycle being 20 min. As shown in Figure 3h, the battery using Pt/C+Ir/C electrode shows a conspicuous charge and discharge voltage decay after 30 cycles (charge–discharge voltage gap of 1.36 V) despite the narrow initial voltage gap (0.9 V), and the degradation continues over time. The voltage gap of the battery using 3DOM-Co@Ti_xON_y electrode increases only 10 mV (from 0.97 to 0.98 V) after 900 cycles (Figure S13, Supporting Information), representing excellent cycling stability with less than 1% energy efficiency loss under highly oxidative operating conditions. As discussed in our design strategy, the excellent activity and durability of 3DOM-Co@Ti_xON_y are attributed to ultrafine Co and its SMSI with the conductive TiO_xN_y support, respectively. Essentially, the OV in TiO_xN_y support as well as its 3DOM structure plays the key role. Thus, we expect its OV and structure should be maintained during OER. To verify this argument, the morphology and composition of the 3DOM-Co@TiO_xN_y upon highly oxidative OER operating conditions (at constant potential of 1.60 V vs RHE) were examined. SEM imaging confirms the 3DOM structure of the composite remained intact after 16 h of OER testing (Figure S14, Supporting Information). Interestingly, the XRD pattern shows its TiON and TiO₂ crystalline disappears, exhibiting only TiO crystal patterns (Figure 1d). Common sense would dictate TiO_xN_y will be eventually oxidized into TiO₂ under OER. Here, we argue that this would be true only in the absence of active OER components. In such cases, the outer surface TiO_xN_y would be “forced” to catalyze OER reaction and gradually oxidized into TiO₂. In fact, there is only a slight oxidation on TiO_xN_y; as shown in the Ti 2p XPS spectrum (Figure 2c, after OER), the low energy Ti 2p_{3/2} peak associated with TiN or TiO disappears. Meanwhile, the intensity of the TiON peak decreases and the TiO_{2-x} (or Ti₂O₃) peak predominates. There is no obvious increase of signal at 459.1 eV (corresponding to TiO₂), indicating its further oxidation is prohibited.

The mild oxidation of TiO_xN_y surface is also consistent with the decrease of the metallic N–Ti peaks (N–Ti–O and N–Ti) intensity in N 1s spectrum (Figure 2e). The oxidation might result from its inevitable involvement in catalyzing OER (Figure 3c). On the other hand, due to its high electrical conductivity, it may receive the electrons released from the active

ultrafine Co during OER, and therefore suppresses its further oxidation. The vanishing of TiO₂ crystal structure in XRD is likely caused by the migration of O²⁻ from inner-core TiO₂ lattice toward the OV-rich TiO_xN_y outer surface, as a consequence of the applied positive voltage in OER. In semiconductor physics, such voltage-driven O²⁻ transportation in defective TiO₂ is well known for resulting to its resistive switching property.^[21] Figure 2d shows that the outer CoO surface of the ultrafine Co nanoparticles was oxidized into Co₃O₄ during OER, indicating Co₃O₄ is the actual catalytic phase for OER. As indicated in the O 1s XPS spectrum, after OER reaction, there is a significant increase in the relative intensity of vacancy O²⁻ and O–C peaks (Figure 2f). The latter confirms the oxidation of carbon layer during OER, whereas the increased intensity of O²⁻ vacancies might have resulted from the positive voltage-induced O²⁻ migration by extracting O²⁻ from the lattice.^[22] Therefore, we conclude that, despite the slight oxidation of the TiO_xN_y surface and carbon layer in the composite, its conductive and OV-rich TiO_{2-x} (or Ti₂O₃) outer surface was preserved during OER. This is the underlying key factor that contributes to the high activity and stability of the composite. Additionally, we found that the chemical state of Co@TiO_xN_y remains almost the same after ORR (Figure S15, Supporting Information), confirming that the stability of ORR/OER bifunctional catalyst is mainly affected by OER rather than ORR.

In summary, building on our improved understanding of OVs in semiconductor physics and its resulting SMSI in solid–gas catalysis, we proposed and demonstrated a rational catalyst design strategy of synthesizing 3DOM-TiO_xN_y semiconductor-supported ultrafine Co as efficient and durable electrocatalyst. Benefiting from the OV-granted features of TiO_xN_y support, including high conductivity, oxidation resistance, and SMSI stabilizing ultrafine Co, the 3DOM-Co@TiO_xN_y composite exhibited comparable ORR-OER performance, but much longer cycling stability than noble metals in a rechargeable zinc–air battery: it achieved over 900 charge–discharge cycles (300 h) at 20 mA cm^{-2} . Moreover, we found that the composite undergoes a composition transition during OER. Such transition helps us elucidate the excellent stability of the composite, which is attributed to the sustained OVs and relative low oxidation state of TiO_xN_y surface during OER reaction. The strategy presented in this study can serve as a fundamental basis for selecting and designing high-performance catalyst support materials for oxygen electrocatalysis in rechargeable zinc–air batteries.

Supporting Information

Supporting Information is available from the Wiley Online Library or from the author.

Acknowledgements

The authors acknowledge the financial support from the Natural Science and Engineering Research Council of Canada (NSERC), the 111 Project (Grant No. D17007), and Henan Center for Outstanding Overseas Scientists (Grant No. GZS2018003). The authors thank Dr. Carmen Andrei and Dr. Andreas Korinek for TEM imaging at the Canadian Center for Electron Microscopy (CCEM) at McMaster University. Part of the

TEM work was performed at the Center for Functional Nanomaterials, Brookhaven National Laboratory, which is supported by the U.S. Department of Energy (DOE), Office of Basic Energy Science, under Contract No. DE-SC0012704.

Conflict of Interest

The authors declare no conflict of interest.

Keywords

bifunctional catalysts, metal–support interactions, oxygen evolution reaction, oxygen vacancies, zinc–air batteries

Received: October 18, 2018

Revised: November 15, 2018

Published online: December 9, 2018

- [1] a) J. Wang, W. Cui, Q. Liu, Z. Xing, A. M. Asiri, X. Sun, *Adv. Mater.* **2016**, *28*, 215; b) Y. Li, M. Gong, Y. Liang, J. Feng, J. E. Kim, H. Wang, G. Hong, B. Zhang, H. Dai, *Nat. Commun.* **2013**, *4*, 1805; c) S. Dresch, F. Luo, R. Schmack, S. Köhl, M. Gliech, P. Strasser, *Energy Environ. Sci.* **2016**, *9*, 2020; d) Z. Zhao, Z. Xia, *ACS Catal.* **2016**, *6*, 1553; e) Y. P. Zhu, C. Guo, Y. Zheng, S. Z. Qiao, *Acc. Chem. Res.* **2017**, *50*, 915; f) G. L. Chai, K. Qiu, M. Qiao, M. M. Titirici, C. Shang, Z. Guo, *Energy Environ. Sci.* **2017**, *10*, 1186; g) G. A. Ferrero, K. Preuss, A. Marinovic, A. B. Jorge, N. Mansor, D. J. L. Brett, A. B. Fuentes, M. Sevilla, M. M. Titirici, *ACS Nano* **2016**, *10*, 5922; h) B. Y. Xia, Y. Yan, N. Li, H. B. Wu, X. W. Lou, X. Wang, *Nat. Energy* **2016**, *1*, 15006; i) Z.-F. Huang, J. Wang, Y. Peng, C.-Y. Jung, A. Fisher, X. Wang, *Adv. Energy Mater.* **2017**, *7*, 1700544.
- [2] a) F. S. Saleh, E. B. Easton, *J. Electrochem. Soc.* **2012**, *159*, B546; b) C. Spçri, J. T. H. Kwan, A. Bonakdarpour, D. P. Wilkinson, P. Strasser, *Angew. Chem., Int. Ed.* **2017**, *56*, 5994.
- [3] a) N. G. Akalework, C. J. Pan, W. N. Su, J. Rick, M. C. Tsai, J. F. Lee, J. M. Lin, L. D. Tsai, B. J. Hwang, *J. Mater. Chem.* **2012**, *22*, 20977; b) G. Zhao, R. Mo, B. Wang, L. Zhang, K. Sun, *Chem. Mater.* **2014**, *26*, 2551; c) A. Lewera, L. Timperman, A. Roguska, N. Alonso-Vante, *J. Phys. Chem. C* **2011**, *115*, 20153.
- [4] a) A. Vesel, M. Mozetic, J. Kovac, A. Zalar, *Appl. Surf. Sci.* **2006**, *253*, 2941; b) B. Avasarala, P. Haldar, *Electrochim. Acta* **2010**, *55*, 9024; c) B. Avasarala, P. Haldar, *Int. J. Hydrogen Energy* **2011**, *36*, 3965.
- [5] a) A. Grimaud, K. J. May, C. E. Carlton, Y.-L. Lee, M. Risch, W. T. Hong, J. Zhou, Y. Shao-Horn, *Nat. Commun.* **2013**, *4*, 2439; b) B. J. Kim, D. F. Abbott, X. Cheng, E. Fabbri, M. Nachttegaal, F. Bozza, I. E. Castelli, D. Lebedev, R. Schaublin, C. Copéret, T. Graule, N. Marzari, T. J. Schmidt, *ACS Catal.* **2017**, *7*, 3245; c) Y. Zhu, W. Zhou, Y. Zhong, Y. Bu, X. Chen, Q. Zhong, M. Liu, Z. Shao, *Adv. Energy Mater.* **2017**, *7*, 1602122.
- [6] a) H. Liu, F. Zeng, Y. Lin, G. Wang, F. Pan, *Appl. Phys. Lett.* **2013**, *102*, 181908; b) X. L. Wang, C. Y. Luan, Q. Shao, A. Pruna, C. W. Leung, R. Lortz, J. A. Zapien, A. Ruotolo, *Appl. Phys. Lett.* **2013**, *102*, 102112.
- [7] a) J. A. Farmer, C. T. Campbell, *Science* **2010**, *329*, 933; b) P. Chen, A. Khetan, F. Yang, V. Migunov, P. Weide, S. P. Stürmer, P. Guo, K. Kähler, W. Xia, J. Mayer, H. Pitsch, U. Simon, M. Muhler, *ACS Catal.* **2017**, *7*, 1197; c) J. C. Matsubu, S. Zhang, L. DeRita, N. S. Marinkovic, J. G. Chen, G. W. Graham, X. Pan, P. Christopher, *Nat. Chem.* **2017**, *9*, 120; d) M.-C. Tsai, T.-T. Nguyen, N. G. Akalework, C.-J. Pan, J. Rick, Y.-F. Liao, W.-N. Su, B.-J. Hwang, *ACS Catal.* **2016**, *6*, 6551; e) I. N. Remediakis, N. Lopez, J. K. Nørskov, *Angew. Chem., Int. Ed.* **2005**, *44*, 1824; f) H.-S. Oh, H. N. Nong, T. Reier, A. Bergmann, M. Gliech, J. F. de Araújo, E. Willinger, R. Schlögl, D. Teschner, P. Strasser, *J. Am. Chem. Soc.* **2016**, *138*, 12552.
- [8] a) D. Yan, Y. Li, J. Huo, R. Chen, L. Dai, S. Wang, *Adv. Mater.* **2017**, *29*, 1606459; b) Y. Guo, Y. Tong, P. Chen, K. Xu, J. Zhao, Y. Lin, W. Chu, Z. Peng, C. Wu, Y. Xie, *Adv. Mater.* **2015**, *27*, 5989.
- [9] a) N. Muthuswamy, M. E. M. Buan, J. C. Walmsley, M. Rønning, *Catal. Today* **2018**, *301*, 11; b) H. T. Chung, D. A. Cullen, D. Higgins, B. T. Sneed, E. F. Holby, K. L. More, P. Zelenay, *Science* **2017**, *357*, 479.
- [10] J. C. Groen, L. A. A. Peffer, J. Pérez-Ramírez, *Microporous Mesoporous Mater.* **2003**, *60*, 1.
- [11] R. L. Kurtz, V. E. Henrich, *Surf. Sci. Spectra* **1998**, *5*, 179;
- [12] a) Q. Zuo, G. Cheng, W. Luo, *Dalton Trans.* **2017**, *46*, 9344; b) H. Jin, J. Li, F. Chen, L. Gao, H. Zhang, D. Liu, Q. Liu, *Electrochim. Acta* **2016**, *222*, 438.
- [13] a) P. O. Larsson, A. Andersson, L. R. Wallenberg, B. Svensson, *J. Catal.* **1996**, *163*, 279; b) B. J. Tan, K. J. Klabunde, P. M. A. Sherwood, *J. Am. Chem. Soc.* **1991**, *113*, 855.
- [14] B. Bharti, S. Kumar, H.-N. Lee, R. Kumar, *Sci. Rep.* **2016**, *6*, 32355.
- [15] M. D. Banus, T. B. Reed, A. J. Strauss, *Phys. Rev. B* **1972**, *5*, 2775.
- [16] U. Kaiser, D. A. Müller, J. Grazul, A. Chuvulin, M. Kawasaki, *Nat. Mater.* **2002**, *1*, 102.
- [17] D. A. Müller, N. Nakagawa, A. Ohtomo, J. L. Grazul, H. Y. Hwang, *Nature* **2004**, *430*, 657.
- [18] T. Zheng, C. Wu, M. Chen, Y. Zhang, P. T. Cummings, *J. Chem. Phys.* **2016**, *145*, 044702.
- [19] a) H. Poppa, *Catal. Rev.* **1993**, *35*, 359; b) M. Che, Z. X. Cheng, C. Louis, *J. Am. Chem. Soc.* **1995**, *117*, 2008.
- [20] a) X. Liu, M. Park, M. Kim, S. Gupta, G. Wu, J. Cho, *Angew. Chem., Int. Ed.* **2015**, *54*, 9654. b) C. Tang, B. Wang, H. F. Wang, Q. Zhang, *Adv. Mater.* **2017**, *29*, 1703185; c) M. Prabu, K. Ketpang, S. Shanmugam, *Nanoscale* **2014**, *6*, 3173.
- [21] N. Ghenzi, M. J. Rozenberg, R. Llopi, P. Levy, L. E. Hueso, P. Stoliar, *Appl. Phys. Lett.* **2015**, *106*, 123509.
- [22] Y. Du, A. Kumar, H. Pan, K. Zeng, S. Wang, P. Yang, A. T. S. Wee, *AIP Adv.* **2013**, *3*, 082107.